Sensitivity of teleseismic body waves to mineral texture and melt in the mantle beneath a mid-ocean ridge

By Donna K. Blackman† and J.-Michael Kendall
Department of Earth Sciences, University of Leeds, Leeds LS2 9JT, UK

Seismic energy propagating through the mantle beneath an oceanic spreading centre develops a signature due both to the subaxial deformation field and to the presence of melt in the upwelling zone. Deformation of peridotite during mantle flow results in strong preferred orientation of olivine and significant seismic anisotropy in the upper 100 km of the mantle. Linked numerical models of flow, texture development and seismic velocity structure predict that regions of high anisotropy will characterize the subaxial region, particularly at slow-spreading mid-ocean ridges. In addition to mineral texture effects, the presence of basaltic melt can cause travel-time anomalies, the nature of which depend on the geometry, orientation and concentration of the melt. In order to illustrate the resolution of subaxial structure that future seismic experiments can hope to achieve, we investigate the teleseismic signature of a series of spreading centre models in which the mantle viscosity and melt geometry are varied. The P-wave travel times are not very sensitive to the geometry and orientation of melt inclusions, whether distributed in tubules or thin ellipsoidal inclusions. Travel time delays of 0.1–0.4 s are predicted for the melt distribution models tested. The P-wave effects of mineral texture dominate in the combined melt-plus-texture models. Thus, buoyancy-enhanced upwelling at a slow spreading ridge is characterized by 0.7–1.0 s early P-wave arrival times in a narrow axial region, while the models of plate-driven-only flow predicts smaller advances (less than 0.5 s) over a broader region. In general S-wave travel times are more sensitive to the melt and show more obvious differences between melt present as tubules as opposed to thin disks, especially if a preferred disk orientation exists. Mineral texture and the preferred alignment of melt inclusions will both produce shear-wave splitting, our models predict as much as 4 s splitting in some cases.

1. Introduction

Decompression of the mantle as it upwells beneath an oceanic spreading centre results in melting of peridotite and the production of basaltic magma. Deformation of peridotite minerals results from viscous shearing of the mantle as it flows in response to plate separation at the ridge axis. Both the presence of lower density melt and the preferred orientation of olivine grains that are strongly anisotropic will influence the seismic signature of the subaxial region. Modelling wave propagation through such

† Present address: Scripps Institute of Oceanography, La Jolla, CA 92093, USA.

Phil. Trans. R. Soc. Lond. A (1997) **355**, 217–231
Printed in Great Britain

TEX Paper

complex anisotropic regions allows us to explore the range of travel time anomalies that would result from previous models of subaxial structure. These predictions illustrate the degree to which surface measurements can provide insight into complexities at depth.

This paper builds on previous work that linked geodynamic modelling, the corresponding development of mineral textures and raytracing through the resultant anisotropic mantle at a mid-ocean ridge (Blackman *et al.* 1997). That paper focused on the seismic effect of flow induced olivine alignment. Our intent here is to complete the self-consistency of the previous models for which the seismic effect of the predicted melt distribution had been ignored. Kendall (1994) made predictions about the travel time signature of some simple subaxial melt models but the assumptions made about melt distribution were only approximate, not directly tied to any specific flow field. Here we improve the assumptions about melt properties, using published values of seismic velocity for basaltic melt and exploring various melt geometries representing a range from evenly distributed 'pores' through films aligned along grain faces.

Current understanding of melt production, segregation and migration through the mantle is incomplete so our approach is to explore several models that bracket physically reasonable melt distributions. This allows us to show that although different melt geometries may produce rather different reductions in local P-wave velocity, the difference in overall travel time anomalies predicted for various cases is rather small. The overall effects for S-waves are slightly larger. Furthermore, significant shear-wave splitting is predicted if the melt lies in vertically aligned thin disk-like inclusions. Detailed results are presented following brief reviews of the geodynamic setting, the observational evidence on melt distribution in the mantle and the theoretical framework for seismic modelling of melt inclusions.

2. Mantle flow and melting at oceanic spreading centres

Spreading of lithospheric plates occurs mainly as a result of forces distant from the axis of a mid-ocean ridge (Forsyth & Uyeda 1975; Houseman 1983) so the assumption that upwelling, at least in the upper 100–200 km of the mantle, is a passive response to plate separation is foremost in our models of subaxial structure. Temperatures in the broad upwelling zone exceed values far off axis by 100–200 °C (Lachenbruch 1973; Sleep 1975; Phipps Morgan & Forsyth 1988). About 70–80 km below the seafloor, the rising peridotite begins to exceed the solidus temperature which increases with depth at a rate of about $3.25\,^{\circ}\mathrm{C\,km^{-1}}$ (see, for example, Hess 1992). The exact nature of the melt as it is initially produced and its mode of migration thereafter is uncertain. The fact that 6–7 km of basaltic crust is steadily produced at the ridge axis (see, for example, Spudich & Orcutt 1980) means that at least this amount eventually migrates to the surface on a time scale appropriate for the local spreading rate. If the melt is retained in the interstices of the residual peridotite then buoyancy forces, due to its lower density, can enhance the upwelling rate of the mantle (melt + matrix) (Rabinowicz *et al.* 1984; Scott & Stevenson 1989). Faster plate spreading rate (i.e. greater passive upwelling rate) and higher mantle viscosity reduce the ability of buoyancy forced flow to dominate the plate driven flow (Parmentier & Phipps Morgan 1990). At slow spreading rates (10–20 $\mathrm{mm\,yr^{-1}}$ half-rate) buoyancy driven flow dominates for asthenosphere viscosity of 5×10^{18} Pa s whereas passive flow dominates for a viscosity of 10^{20} Pa s (figure 1).

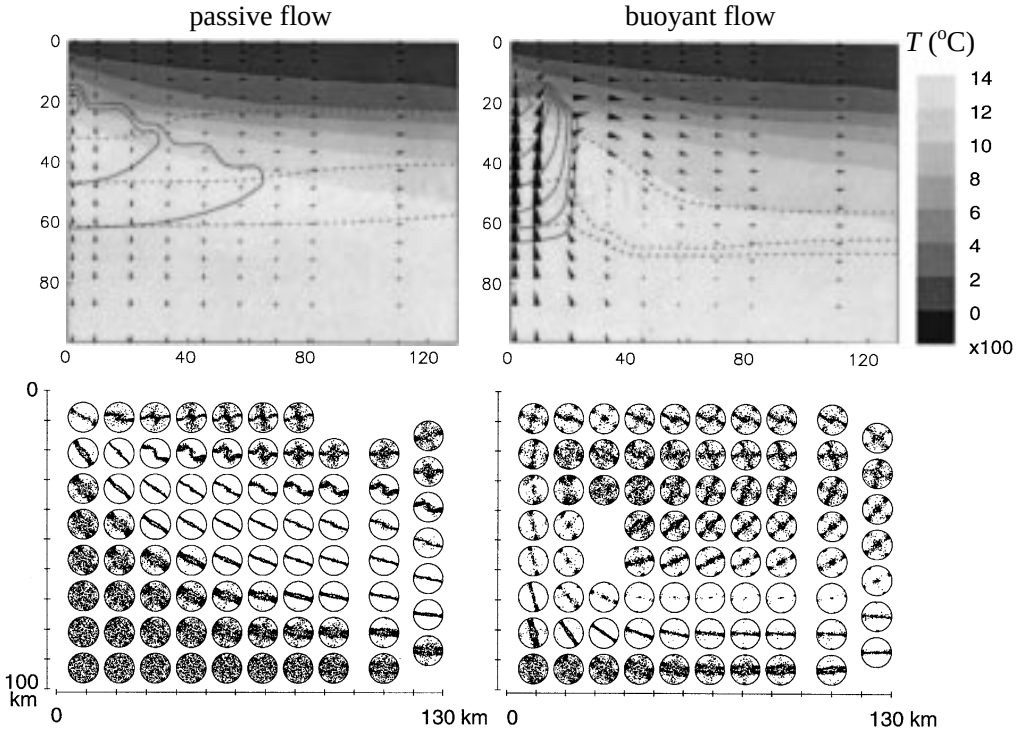

Figure 1. Models of mantle structure beneath a slow-spreading mid-ocean ridge; axis is at left in diagrams. Top panels show flow vectors scaled by rate of flow, 18 mm yr^{-1} half spreading rate is shown by arrowheads in the lithosphere (less than 700 °C indicated by shading). Plate driven flow dominates when asthenosphere viscosity is 10^{20} Pa s (left panels). Buoyancy forces, due to the presence of melt, enhances upwelling rates, which causes focusing towards the axis, when viscosity is 5×10^{18} Pa s (right panels). Solid contours show melt at increments of 1% volume fraction. Up to 6% melt fraction is generated in the buoyant model compared with a maximum of 3% in the passive flow model. Dashed contours show upwardly increasing degree of depletion in the residual mantle due to the removal of melt. Equal-area projection pole figures in the lower panels show the orientation of seismically fast *a*-axis for olivine crystals within an aggregate at each grid point. Mineral texture is random at 100 km depth but preferred orientations develop as the aggregates are subjected to the strain field of the flow model shown in the top panels (Blackman *et al.* 1997; Chastel *et al.* 1993). Pole figure girdles indicate the orientation of the plane in which the *a*-axes align, the slow *b*-axis orients perpendicular to this plane. In the passive case, the fast plane subparallels the base of the lithosphere; in the buoyant case strong vertical alignment develops beneath the ridge axis and high shearing due to focussing of the flow results in a layer of subhorizontal a-axis planes that are rafted off axis at depth.

The question of how much melt is retained in the matrix has seismic ramifications not only in terms of the melt distribution itself but also in terms of the development of preferred orientation in olivine since the deformation field is quite different for passive versus buoyancy enhanced flow. If the melt migrates essentially immediately, as suggested by recent geochemical modelling (McKenzie 1984; O'Nions & McKenzie 1993; Spiegelman 1996), melt may not significantly influence the mantle flow pattern. If volume fractions up to 1–2% are retained and asthenosphere viscosity is on the order of 10^{18} Pa s, some buoyancy driven flow will still evolve. There continues to be some debate about subaxial mantle viscosity structure (Karato 1986; Kohlstedt 1992; Hirth & Kohlstedt 1992, 1996) and the degree of melt retention (see, for example, Waff & Holdren 1981; Waff & Faul 1992). Therefore, it is useful to illustrate the

seismic signatures that would result from both passive and buoyancy enhanced flow models and to investigate how their differing melt distributions and deformation fields affect the seismic predictions.

Whether melt is retained until shallower depths (10–20 km) or is segregated and migrates immediately, the geometry of the melt inclusions as they form and the mode of melt transport will affect the nature of wave propagation through the melt zone. Interconnected tubules of melt distributed along grain intersections (Waff & Bulau 1982; Toramaru & Fujii 1986) allow melt transport via porous flow and may reduce isotropic P- and S-wave velocities. In contrast, a network of fractures transporting melt (Nicolas 1989; Nielson & Wilshire 1993; Ceuleneer *et al.* 1996) may produce an anisotropic signature, particularly if the fractures are aligned (next section). Nielson & Wilshire (1993) note that clear evidence for melt transport via large scale percolation has not yet been found but Quick & Gregory (1995) comment that the networks of dykes observed in ophiolites probably represent the shallow levels of the magma supply system rather than its base. Again, we investigate the seismic signature of a range of possible melt geometries: evenly distributed melt, representing porous flow; melt in thin tubules such as might occur at grain edges; and disk-like inclusions that can be aligned, representing melt-filled fracture planes or melt films that mimic interconnected networks when the aspect ratio is large.

3. Modelling the effect of melt on seismic properties

The effects of melt on seismic waves are not only a function of melt fraction, but also a strong function of the melt inclusion geometry and orientation. Experimental studies of melting in peridotites have yet to come to consensus on melt geometry (cf. Schmeling 1985; Forsyth 1992). Melt may lie along grain faces and can be approximated by ellipsoidal inclusions, it may reside in interconnected tubules along grain edges, or it may reside in melt pockets. In order to isolate their seismic responses we treat each in isolation.

Five possible melt orientations and geometries are considered. The first is a simple isotropic reduction of velocities which is obtained from a scaled combination of the host rock velocities and the melt velocities which is controlled by the melt-fraction (hereafter referred to as the *scaled* model).

The next two models consider the melt to be in 'penny-shaped' inclusions. Support for this comes from experimental work with ultramafic partial melts by Waff & Faul (1992) and Faul *et al.* (1994). They found that more than 75% of the melt occurred in ellipsoidal inclusions with small aspect ratios. O'Connell & Budiansky (1974) and Schmeling (1985) showed that these inclusions can be approximated as oblate spheroids (disks) when estimating their effects on elastic properties. We adopt the approach of Hudson (1980) to estimate effective elastic constants of material filled with such disk-like inclusions. We use the Hudson (1980) expressions which are accurate to second order in $\varepsilon = Na^3/V$ (where N is the number density of the inclusions, a is the mean radius of the inclusions and V is volume). The theories of O'Connell & Budiansky (1977) and Schmeling (1985) are more accurate than Hudson (1980), but they are only valid for randomly oriented inclusions and we are interested in potential anisotropic effects due to the alignment of such inclusions. Furthermore, the crack densities and aspect ratios we consider are within the accuracy limits of the Hudson (1980) theory. We consider the isotropic case of randomly aligned disks (*random disks*) and the anisotropic case of disks aligned with the disk-face

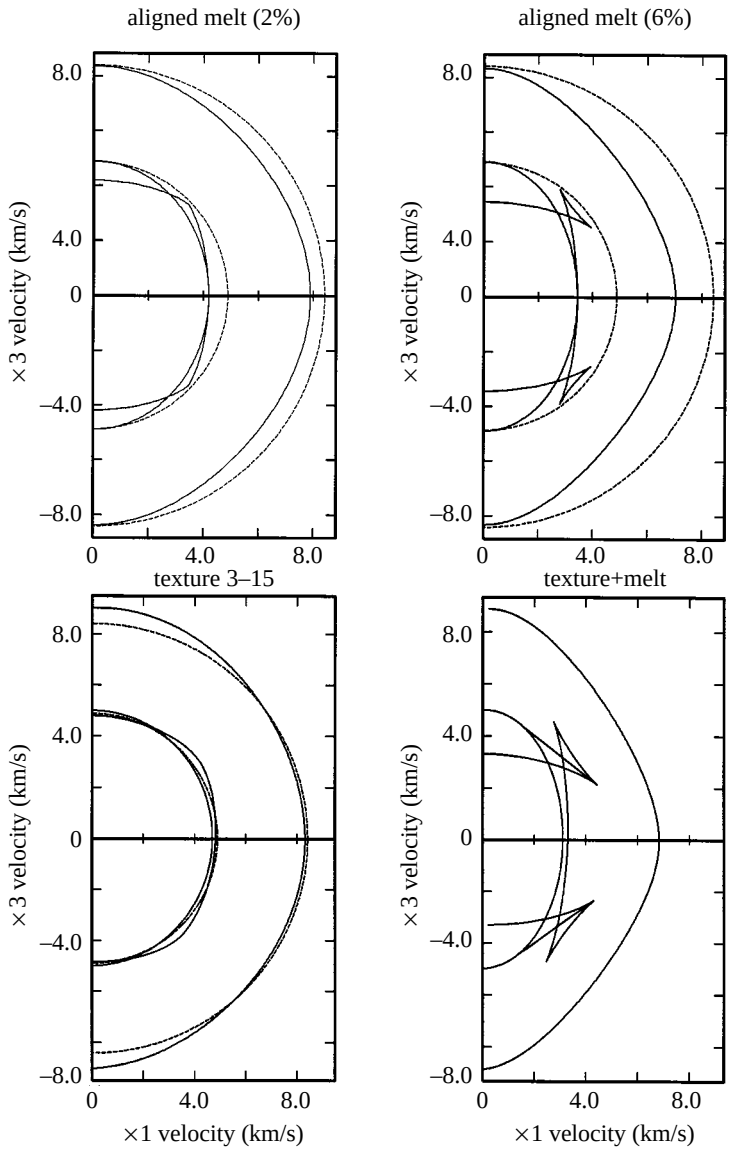

Figure 2. Wave surfaces predicted for anisotropic melt and texture models; point source at 0, 0 for each plot. The dashed lines show the P- (outer) and S- (inner) surfaces for a reference isotropic model of randomly oriented olivine crystals. Upper panels: melt distributed in disk-like inclusions with the normal to the disk-face oriented in the direction of plate spreading. Melt fractions of 0.02 and 0.06 are shown. Lower left: anisotropy due to the lattice preferred orientation of olivine crystals predicted 3 km off axis and 15 km deep for the buoyant flow model (Blackman *et al.* 1997). Lower right: combined effect of oriented olivine and aligned melt inclusions (6% melt). Note the development of S-wave triplications as the melt fraction increases. In the melt models the vertically travelling S-wave polarized normal to the inclusion faces will be slower than that polarized parallel to the faces, which, like the vertically travelling P-wave, is largely unaffected by the aligned melt.

normals oriented in the direction of plate spreading (*aligned disks*). Support for such an orientation comes from the theoretical studies of Phipps Morgan (1987) and Spiegelman (1993).

The final type of inclusion we consider is the tubule which we approximate as a cigar shaped spheroid. Mavko (1980) and others consider the effects of tubules with circular and non-circular cross-sections. Schmeling (1985) showed that the range of possible tubule shapes give similar results to those for ellipsoidal inclusions with aspect ratios between 0.2 and 0.5 (i.e. not very flat). The elastic moduli are not very sensitive to this range of variations in aspect ratio so we feel it representative to only consider tubules with circular cross-sections. We are interested in the effects of randomly oriented tubules (*random tubules*) and tubules with vertically oriented major-axes (*aligned tubules*). The theory of Tandon & Weng (1984) and Sayers (1992) is used to estimate the effective elastic constants for the situation of oriented tubule inclusions. We use a Voigt average of these elastic constants to estimate the elastic moduli for random orientations of the tubules.

We assume that the matrix rock has the elastic properties of randomly oriented olivine, $v_{\mathrm{P}} = 8421\,\mathrm{m\,s^{-1}}$, $v_{\mathrm{S}} = 4487\,\mathrm{m\,s^{-1}}$ and density $= 3311\,\mathrm{kg\,m^{-3}}$ (velocities are obtained using Voigt–Ruess–Hill averages for the elastic constants of Kumazawa & Anderson (1969)). The assumed melt properties are $v_{\mathrm{P}} = 2500\,\mathrm{m\,s^{-1}}$, $v_{\mathrm{S}} = 0$ and density $= 2700\,\mathrm{kg\,m^{-3}}$ (Murase & McBirney 1973). Based on the measurements of Faul *et al.* (1994) we use an aspect ratio of 0.05 for the disks. The aspect ratio is defined as the height of the oblate spheroid to its radius. Thus disks have an aspect ratio less than one while tubules are greater than one. The assumed aspect ratio for the tubules is 20. The maximum melt fraction in the buoyancy case is 0.06 which corresponds to an inclusion density of 0.38.

Wavefronts for some of the models we consider are shown in figure 2. As the percentage of melt increases, the velocities decrease and if the melt lies in oriented inclusions the anisotropic effects can be quite dramatic. For vertically aligned disk-like inclusions of melt, the S-wavefronts can develop triplications as the melt fraction increases. The S-wave which is polarized perpendicular to the disk faces will be affected the most, just as P-waves propagating normal to the disk face will be slower than those propagating parallel to the disk faces. Figure 2 also shows the wave surfaces for a region of the texture models with fairly high degree of alignment of olivine crystals. The combination of melt inclusion alignment and mineral alignment produces complex S-wave surfaces.

We have not considered the effects of attenuation or the effects of inclusions being hydraulically connected (sometimes known as 'melt-squirt' (Mavko & Nur 1975)). For waves travelling nearly parallel to the inclusion faces, which is the direction of wave propagation we are considering, such melt interconnectivity is expected to have negligible effects (Thomsen 1995).

The theories for estimating the effective elastic properties of partial melt assume the melt has a spatial distribution which is small compared to the seismic wavelength. It is not possible to distinguish between melt in large but sparse inclusions and melt in many small inclusions.

4. Results

(*a*) *Influence of melt on velocities*

The velocity dependence on geometry, orientation and concentration of the melt is shown in figure 3. Randomly oriented disks (flat ellipsoidal inclusions) have the largest effect on P-wave velocities and both the P- and S-velocities are sensitive to the aspect ratio (figure 3, Schmeling 1985). If the disks are vertically aligned, the

vertically travelling P-wave shows little sensitivity to the inclusions regardless of the aspect ratio. Likewize, the vertically travelling S-wave polarized parallel to the disk faces is not sensitive to the melt. Considerable shear-wave splitting is possible, though, as the orthogonally polarized S-wave is very sensitive to the melt.

Velocities for the tubule model are not very sensitive to the aspect ratio of the tubules. Randomly oriented tubules have a larger effect on the P-wave velocity in the vertical direction than that due to aligned tubules. The S-waves are not sensitive to the alignment or aspect ratio of the tubules and agree well with the results of simply scaling the melt and matrix S-velocities with a melt-fraction weight average. The vertically aligned tubules will not produce splitting in vertically travelling S-waves.

The curves in figure 3 are in line with previous laboratory and theoretical studies. Faul *et al.* (1994) compute 1.8% and 3.3% reductions in P- and S-wave velocity, respectively, for a melt geometry (penny-shaped ellipses) representing thin films along grain boundaries versus 1% and 2.3% reductions for a geometry (cigar shaped ellipsoids) representing melt along grain edges.

It is important to note that although one model of melt geometry may predict an effective velocity of the melt + matrix that is reduced more than twice as much as another model, all models predict changes of the order of a few percent. Dramatic as 'twice the reduction' may sound, it is the accumulation of travel time delay during transit through the melt zone, which extends on the order of a few tens of kilometres and in which v_{P} is about $8\,\mathrm{km\,s^{-1}}$ ($4\,\mathrm{km\,s^{-1}}$ for S-waves), that will be measured at the surface.

(*b*) *Travel time predictions for melt-only models*

Asymptotic ray theory is used to track wavefronts through three dimensional models which have up to 21 independent elastic constants (Kendall & Thomson 1989; Guest & Kendall 1993). The travel time delays due to the subaxial melt fractions predicted by the passive and buoyant flow models primarily reflect the amount of melt present and the overall shape of the melt regions. For all melt geometries, the maximum delay is at the axis and the delay for the passive model is less than half that predicted for the buoyant model. This mainly reflects the fact that melt fractions in the passive model are generally 1–2%, reaching 3% only in a narrow axial region at the top of the melt zone. In the buoyant model values of 2–5% are characteristic and 6% melt fractions are reached at 18–25 km depths within 18 km of the axis (figure 1).

The largest travel time delay for near-vertical P-waves is produced by the randomly oriented melt-filled disks. Arrivals at the axis are predicted to be 0.13 s and 0.33 s later than off-axis arrivals for the passive and buoyant cases, respectively (figure 4). In contrast, aligned disks produce the least P-wave travel time delay for near vertical rays. The travel times for random and aligned disks bracket the case where the velocity is a simple scaling of the melt and matrix velocities. The difference between the predicted travel times for the disk and tubule models is less than 0.1 s for the P-waves and would generally not be resolvable in teleseismic signals recorded at the seafloor (Blackman *et al.* 1995). In summary, near-vertical P-waves propagating through randomly oriented inclusions are more strongly affected by the melt than P-waves traveling vertically through a medium with vertically aligned melt inclusions.

The S-wave travel time delays for the melt geometries that produce an isotropic medium are at least three times as great as the P-wave delays (figure 4, lower panels). The aligned disks produce significant shear wave splitting. The slowest S-wave

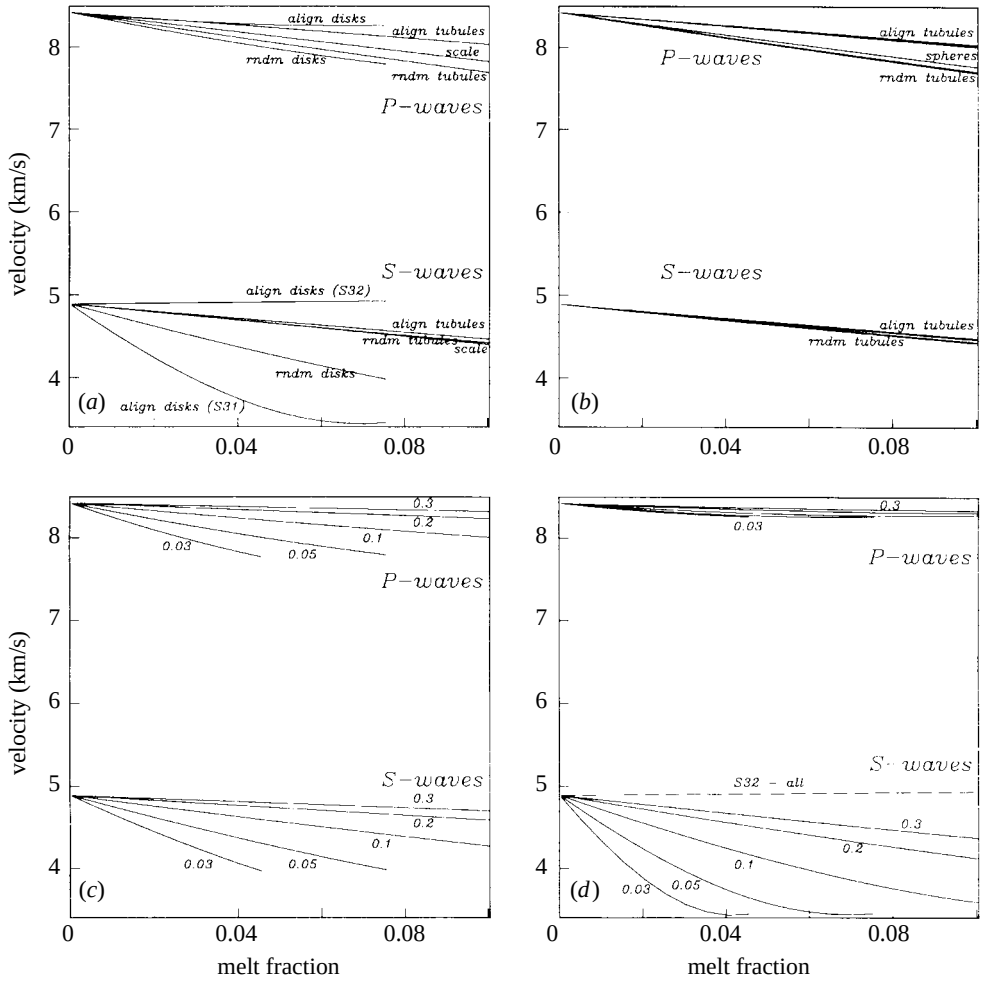

Figure 3. Effects of melt inclusion geometry on seismic velocity as a function of melt fraction. All models have a background matrix of randomly oriented olivine crystals. (*a*) Comparison of models: disk models, both vertically aligned and randomly oriented, have an aspect ratio of 0.05. When disks are aligned vertically, anisotropic velocities for vertically travelling waves are shown. The S-wave polarized normal to the disk faces is denoted $S31$ while that polarized parallel to the face is denoted $S32$. Velocities are plotted only in regions where the disk theory (Hudson 1980) is valid. The tubules have an aspect ratio of 20. The case where the velocities are determined simply from a melt-fraction weighted average of the melt and matrix velocities is marked *scale*. (*b*) Randomly aligned and vertically aligned tubules models. Aspect ratios of 100, 20, 10, 5 and 1 (spheres) are considered, but only for the case of P-waves traveling through media with spherical inclusions is there discernable difference between models. (*c*) Randomly oriented disks modelled with aspect ratios of 0.03, 0.05, 0.1, 0.2 and 0.3. (*d*) Vertically aligned disks with various labelled aspect ratios. The results for S-waves polarized perpendicular to the cracks are shown in solid lines while the results for S-waves polarized parallel to the disks plot on a single line for all models (dashed and marked $S32$). Note the evidence of the Hudson theory breaking down at small aspect ratio and high melt fractions (e.g. aspect ratio of 0.03 and melt fraction of 0.04).

(polarized perpendicular to the disk faces) arrives 1.7 s (passive) and 4.2 s (buoyant) later at the axis than the fastest S-wave (polarized parallel to the disk faces). This is

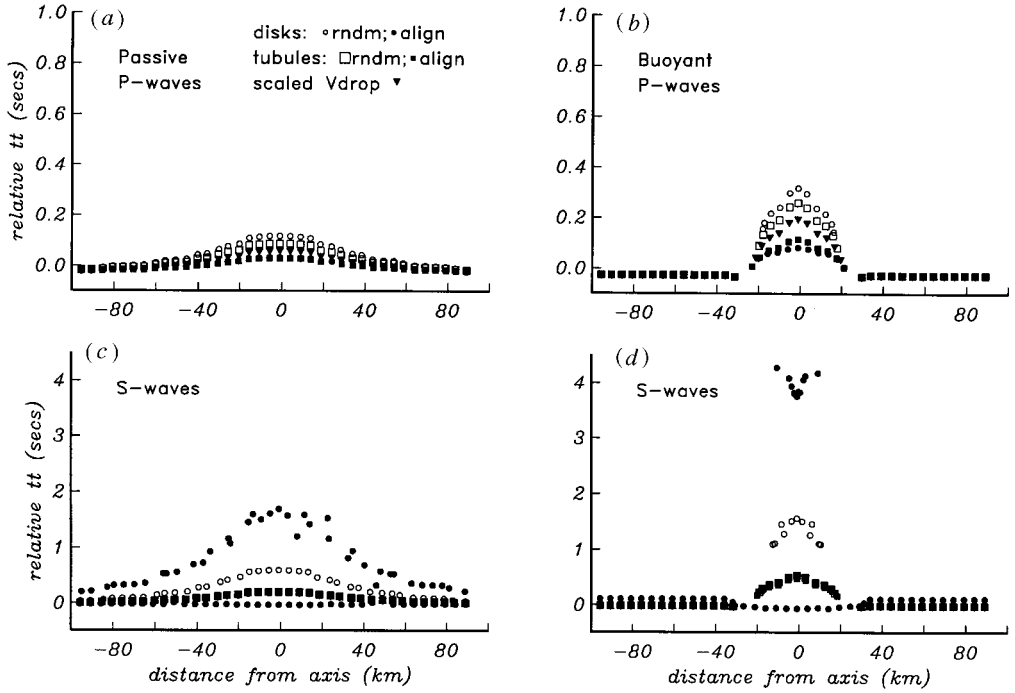

Figure 4. Relative travel times of near-vertical rays that transit subaxial mantle models containing basaltic melt (solid contours in figure 1) within homogeneous, isotropic olivine: passive flow model (left), buoyant flow model (right), P-wave travel times (upper panels), and S-wave travel times (lower). Predictions for different models of the geometry of melt within the matrix (see text) are indicated by different symbols as labelled. Maximum P-wave delay at the axis occurs for randomly oriented melt disks. Maximum S-wave delay occurs at the axis as well and is accompanied by shear-wave splitting if melt-filled disks are vertically aligned. Delay magnitudes are greater in the buoyant model which has higher melt fractions and a narrower melt zone than the passive flow model. The minor travel time advance at the axis for the fast shear wave (S32) in the aligned disk case is due to the effective density of the melt zone being lower than that in the off-axis region while the elasticity for this polarization is largely unaffected by the melt (velocity is proportional to the elasticity divided by the density).

the maximum possible splitting as it assumes all of the melt lies in aligned disk-like inclusions.

The models are parametrized on a regularly spaced grid. In regions where the melt fraction changes quickly there is a degree of roughness in the spline interpolation of the elastic constants for the models. Some of the scatter in the travel times can be attributed to this, but most is due to the complex ray trajectories which result from wave propagation through regions with sharp velocity gradients. Nevertheless, the overall features of the travel time curves are robust.

Rays travelling from teleseismic events at ranges greater than about 90° will be near vertically incident on the seafloor at a mid-ocean ridge but rays from events at closer range will arrive at shallower angles. Figure 5 shows the predicted P-wave travel time anomalies for the suite of melt geometry models for both the passive and buoyancy enhanced flow cases. The waves propagate in a left to right sense and have an initial trajectory 30° from the vertical at the bottom of the model. As expected, the relative travel times across the profile are asymmetric with respect to the ridge axis but the maximum delay is still at the axis. This is due to the effects

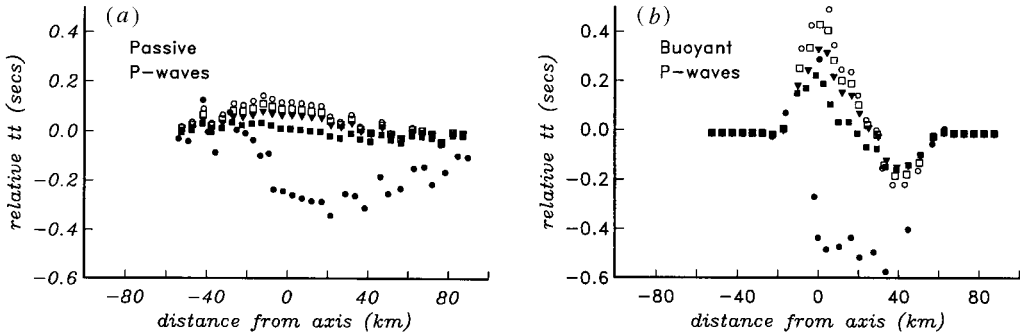

Figure 5. Relative travel times of P-waves incident at 30° from vertical, travelling from left to right, for the passive (*a*) and buoyant (*b*) models of subaxial melt distribution. Velocity structure is the same as in figure 4 as are symbols indicating different melt geometry models. See text for discussion of travel time advance for vertically aligned melt-filled disk case (solid circles).

of ray bending towards the lower axial velocities. The size of the axial delay for the passive case is slightly greater than that predicted for near-vertical arrivals, but it is more than twice as great in the buoyant case. Early travel times are predicted in the axial region to the right of the ridge axis (roughly 0–50 km off axis) for all melt geometry models in the buoyant case. Only the aligned disk model produces such a travel time advance in the passive model. Although it is initially surprising to see early arrivals for rays that transit the melt zone, the signal is a result of rays being refracted into the lower-velocity axial region thereby shortening the raypaths and travel times. The velocity gradients are the most extreme in the aligned disk model due to the significant anisotropy.

The travel time patterns for S-waves propagating with initial take-off angles of 30° are not shown, but are similar to those for the P-waves. The isotropic models show an asymmetry about the axis, but the near-axis delays and advances are more pronounced due to the slower S-wave velocities. The buoyant case, for example, shows up to 1 s delay to the source-side of the axis and 0.3 s advance on the other side of the axis. The anisotropic aligned-disk models show large degrees of shear-wave separation. The fast S-wave for the passive case is roughly 0.3 s early at the axis, whilst the slow S-wave is over 2.2 s late compared to the off axis arrivals. Predictions for the buoyant model show much larger and more complex effects.

(*c*) *Travel time predictions for melt + texture models*

We now combine the effects of mineral texture (Blackman *et al.* 1997) and melt distribution. Near vertical P-waves that propagate through the texture models (anisotropy due to mineral alignment) arrive at the axis earlier than off axis (lower curves in the top panels of figure 6). The axial advance in the passive case is about 0.5 s relative to 50 km off axis. The axial advance in the buoyant case is more dramatic, reaching 1.0 s relative to the same distance off axis. For both models the off axis delay reflects textural anisotropy in which the slow direction for P-waves is near vertical as illustrated in figure 1 (see Blackman *et al.* (1997) for more complete discussion). The greater P-wave advance of the buoyant axial arrivals, relative to the passive case, also reflects the vertical alignment of the plane of fast olivine axes due to focusing and enhancement of the upwelling. Blackman *et al.* (1993, 1995) present sparse data from a teleseismic experiment on the southern Mid-Atlantic Ridge that

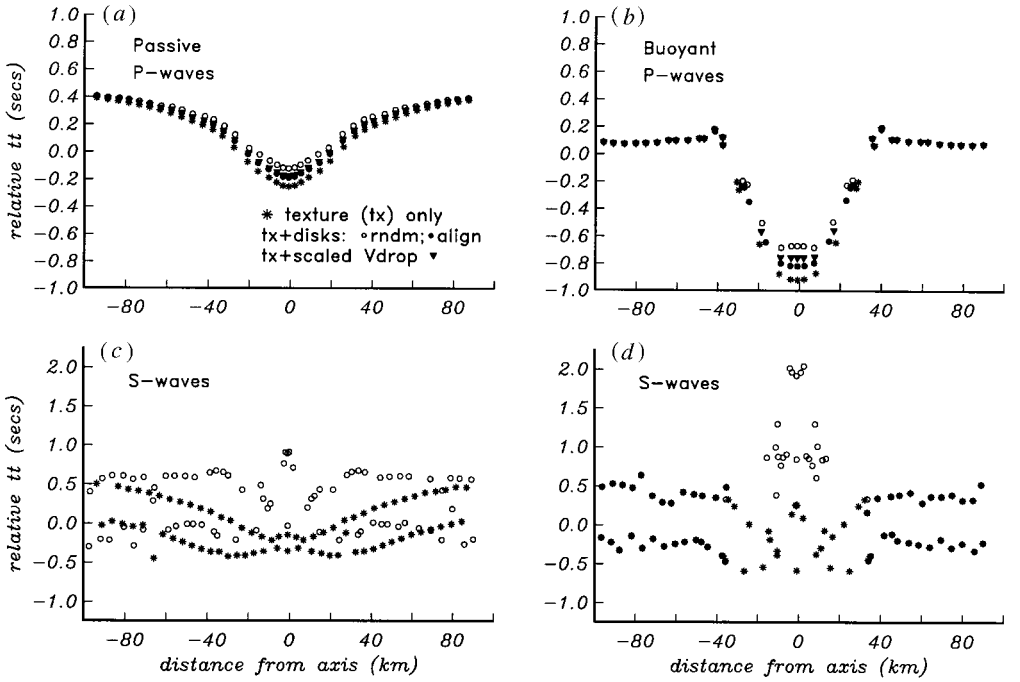

Figure 6. Relative travel times of near-vertical rays through combined melt + textural anisotropy models of subaxial structure for passive (left panels) and buoyant (right panels) flow model. P-waves arrive on axis earlier than off axis due to preferred orientation of olivine crystals (figure 1) which slows vertical propagation off axis and, in the buoyant case, speeds vertical propagation below the axis. Addition of melt to the texture models reduces the size of the axial travel time advance a small amount for P-waves. An axial S-wave delay overprints the texture-only (∗) signal as illustrated for the randomly oriented melt disk geometry (open circles). The shear-waves polarized perpendicular to the ridge axis are the late arrivals off axis (—∗—), but they are earliest to arrive at the ridge axis.

suggests that travel time delays may indeed increase with distance from the ridge axis for stations located outside the median valley.

Combinations of the melt models discussed in the previous section and the textural anisotropy models illustrate the relative importance of each mechanism on travel times. For P-waves in the melt alone models, randomly oriented disks of melt in the buoyant model can produce axial delays up to 0.4 s. The P-wave results for the combined textural and melt models (upper panels of figure 6) show that the texture effects dominate. The relative axial delay due to the melt is muted by the off-axis delays due to the horizontal alignment of the a-axis of olivine. For the models tested, the reduction in the texture-controlled early axial travel times caused by presence of melt is less than 0.3 s for the buoyant case and less than 0.1 s for the passive case.

Rays paths for S-waves in the combined melt + texture models can be complicated but the overall pattern found for the texture travel times is evident for the combined models. The polarity of the fastest arriving shear wave off axis is opposite that of the earliest S-wave at the axis (figure 6, lower panels). The amount of predicted shear wave splitting is greater in the buoyant case than in the passive case where the axial splitting would probably not be resolvable in data. Addition of melt distributed in randomly oriented melt-filled disks to the texture model modifies the axial S-wave travel time anomaly in a fashion that is predictable from the melt-only model. An

axial delay of up to 2.5 s is predicted for the buoyant model, whereas for the passive model the relative delay is quite a bit smaller due to the lower melt fractions. The amount of shear wave splitting at the axis increases somewhat over the texture-only model even though the randomly oriented disk model does not give anisotropic elastic constants. This is simply because there is an overall reduction of velocity in the melt zone therefore S-wavefronts have more time to accrue separation.

5. Discussion

The travel time delay that we predict to be associated with a given melt model depends on our initial assumption that the melt produced during upwelling is retained in the interstices of the matrix during most of the mantle ascent beneath a spreading centre. This is useful in that it allows us to estimate the maximum effect that melt in a series of distribution models might have on teleseismic travel times. If melt migrates rapidly upon production or does not accumulate to more than 1% volume fraction then the melt-related axial delay can only be smaller than what we predict.

Currently, teleseismic data with enough resolution to detect a delay associated with subaxial melt is limited. Forsyth (1997) reports that ocean bottom hydrophones deployed on the Mid-Atlantic Ridge 35° N recorded PKP arrivals that show a relative travel time delay that can be attributed to the presence of a narrow melt zone about 20–30 km deep beneath the spreading centre. Stations located within the median valley had travel time delays, after correction for variable topography and range differences between stations, up to about 0.3 s relative to stations located 16 km off axis. The size of this signal is close to our predictions for the buoyancy enhanced flow model with up to 6% melt fraction distributed in randomly oriented disks or tubules. The narrowness of the travel time anomaly observed by Forsyth (1997) would suggest that melt is more focused than our flow modelling predicts. Blackman *et al.* (1995) note that there may be a 0.2 s P-wave delay for a central American earthquake that is received by an ocean bottom seismometer 10 km west of the East Pacific rise axis. It is possible that the delay is due to melt in the mantle beneath the ridge axis but the experiment geometry does not allow local heterogeneity at the station to be ruled out.

Melt distributed in aligned disk-like inclusions has the largest effect on near vertical shear waves that transit the subaxial region but this reflects the fact that the plane of the disks are oriented vertically. A different alignment would produce different results. It is not certain that melt films will preferentially occupy grain faces that are vertical in the upwelling zone but Phipps Morgan (1987) and Spiegelman (1993) show that melt paths should be near vertical in this region if pressure gradients and oriented permeability in the matrix control the migration. If melt occupies an interconnected network it is reasonable to assume that the films along faces that are not oriented vertically will migrate towards the vertical faces if the pressure drop that is driving upward flow of melt along the vertical faces is sufficient. At a larger scale, this type of behaviour is predicted (Sleep 1984) and observed (Ceuleneer & Rabinowicz 1992; Takahashi 1992) where vertical dykes or melt-filled fractures drain regions of lower melt fraction.

The travel time contributions of lithospheric velocity structure and crustal structure have been ignored in our calculations in order to emphasize the effect of the melt and the textural anisotropy. Thermal heterogeneity in the mantle is included

indirectly in terms of the location and presence of the melt zone. An additional thermal signal due to the small decrease in velocity between the cool lithosphere and the underlying asthenosphere would reduce the predicted delays 100 km off axis by less than 0.1 s and 0.4 s, for P- and S-waves, respectively (Kendall 1994). Oceanic crustal structure is generally rather uniform compared to the continents (Spudich & Orcutt 1980) but variations in its thickness and density structure do occur. Differences in crustal thickness of 3 km (see, for example, Michael *et al.* 1994; Tolstoy *et al.* 1993) across the profile for which we predict travel time anomalies would introduce less than 0.25 svariations. The axial region is generally highly fractured and hydrothermal circulation may occur to depths of a few kilometres. The observed axis-parallel orientation of most median valley fissures would result in significant crustal anisotropy at the shallowest levels. MacDonald *et al.* (1994) report more than 50% anisotropy in the upper few hundred metres of the crust at the Juan de Fuca ridge. To get a rough estimate of the shear-wave splitting effects due to crustal anisotropy we assume the velocities and anisotropy reported in MacDonald *et al.* (1994) throughout a 1 km thick region of aligned fractures at the ridge axis. Shear wave splitting of about 0.4 s would result. This is less than 20% of the splitting magnitude that we predict to occur for mantle melt fractions of about 2% distributed in vertically oriented disks.

The modelling shows that clear P- and S-arrivals with a range of slownesses are required to discriminate between passive and buoyancy driven flow using ocean-bottom teleseismic observations. Probably the most robust feature of the models is the style of anomalous travel time behaviour across the axis. The buoyant case is characterized by larger travel time effects in a narrower axial region, while the passive case shows smaller effects over a broader axial region. Inferring the geometry of melt inclusions will be difficult, especially with P-wave data. Our predictions indicate that S-waves will show more obvious differences between melt stored in tubules rather than disks especially if a preferred disk orientation exists. Untangling these effects from those due to mineral alignment will require high quality and well distributed data.

References

Blackman, D. K., Orcutt, J. A. Forsyth, D. W. & Kendall, J.-M. 1993 Seismic anisotropy in the mantle beneath an oceanic spreading center. *Nature* **366**, 675–677.

Blackman, D. K., Orcutt, J. A. & Forsyth, D. W. 1995 Recording teleseismic earthquakes using ocean bottom seismographs at mid-ocean ridges. *Bull. Seism. Soc. Am.* **185**, 1648–1664.

Blackman, D. K., Kendall, J.-M., Dawson, P. R., Wenk, H.-R., Boyce, D. & Phipps Morgan, J. 1997 Teleseismic imaging of subaxial flow at mid-ocean ridges: travel time effects of anisotropic mineral texture in the mantle. *Geophys. J. Int.* (In the press.)

Ceuleneer, G. & Rabinowicz, M. 1992 Mantle flow and melt migration beneath oceanic ridges: models derived from observations in ophiolites. In *Mantle flow and melt generation at mid-ocean ridges* (ed. J. Phipps Morgan *et al.*), pp. 123–154. (Geophysical Monograph 71.) Washington, DC: AGU.

Ceuleneer, G., Monnereau, M. & Amri, I. 1996 Thermal structure of a fossil mantle diapir inferred from the distribution of mafic cumulates. *Nature* **379**, 149–153.

Chastel, T. B., Dawson, P. R., Wenk, H.-R. & Bennett, K. 1993 Anisotropic convection with implications for the upper mantle. *J. Geophys. Res.* **98**, 17 575–17 771.

Faul, U. H., Toomey, D. R. & Waff, H. S. 1994 Intergranular basaltic melt is distributed in thin, elongated inclusions. *Geophys. Res. Lett.* **21**, 29–32.

Forsyth, D. W. & Uyeda, S. 1975 On the relative importance of the driving forces of plate motion. *Geophys. Jl R. Astr. Soc.* **43**, 163–200.

Forsyth, D. W. 1992 Geophysical constraints on mantle flow and melt generation beneath mid-ocean ridges. In *Mantle flow and melt generation at mid-ocean ridges* (ed. J. Phipps Morgan *et al.*), pp. 103–122. (Geophysical Monograph 71.) Washington, DC: AGU.

Forsyth, D. W. 1997 Partial melting beneath a Mid-Atlantic Ridge segment detected by teleseismic PKP delays. *Geophys. Res. Lett.* (In the press.)

Guest, W. S. & Kendall, J.-M. 1993 Modelling waveforms in anisotropic inhomogeneous media using ray and Maslov theory: applications to exploration seismology. *Can. J. Expl. Geophys.* **29**, 78–92.

Hess, P. C. 1992 Phase equilibria constraints on the origin of ocean floor basalts. In *Mantle flow and melt generation at mid-ocean ridges* (ed. J. Phipps Morgan *et al.*), pp. 67–102. (Geophysical Monograph 71.) Washington, DC: AGU.

Hirth, G. & Kohlstedt, D. L. 1992 Experimental constraints on the dynamics of the partially molten upper mantle: deformation in the diffusion creep regime. *J. Geophys. Res.* **100**, 1981–2001.

Hirth, G. & Kohlstedt, D. L. 1996 Water in the oceanic upper mantle: implications for rheology, melt extraction and the evolution of the lithosphere. *Earth Planet. Sci. Lett.* **144**, 93–108.

Houseman, G. 1983 The deep structure of ocean ridges in a convecting mantle. *Earth Planet. Sci. Lett.* **64**, 283–294.

Hudson, J. A. 1980 Overall properties of a cracked solid. *Math. Proc. Camb. Phil. Soc.* **88**, 371–384.

Karato, S. 1986 Does partial melting reduce the creep strength of the upper mantle? *Nature* **319**, 309–310.

Kendall, J.-M. 1994 Teleseismic arrivals at a mid-ocean ridge: effects of mantle melt and anisotropy. *Geophys. Res. Lett.* **21**, 301–304.

Kendall, J.-M. & Thomson, C. J. 1989 A comment on the form of the geometrical spreading equations, with some examples of seismic ray tracing in inhomogeneous, anisotropic media. *Geophys. J. Int.* **99**, 401–413.

Kohlstedt, D. 1992 Structure, rheology and permeability of partially molten rocks at low melt fractions. In *Mantle flow and melt generation at mid-ocean ridges* (ed. J. Phipps Morgan *et al.*), pp. 103–122. (Geophysical Monograph 71.) Washington, DC: AGU.

Kumazawa, M. & Anderson, O. L. 1969 Elastic moduli, pressure derivatives and temperature derivatives of a single-crystal olivine and a single crystal forsterite. *J. Geophys. Res.* **74**, 5961–5972.

Lachenbruch, A. 1973 A simple mechanical model for oceanic spreading centers. *J. Geophys. Res.* **78**, 3395–3417.

MacDonald, M. A., Webb, S. C., Hildebrand, J. A., Cornuelle, B. D. & Fox, C. F. 1994 Seismic structure and anisotropy of the Juan de Fuca ridge at 45° N. *J. Geophys. Res.* **99**, 4857–4873.

Mavko, G. M. & Nur, A. 1975 Melt squirt in the asthenosphere. *J. Geophys. Res.* **80**, 1444–1448.

Mavko, G. M. 1980 Velocity and attenuation in partially molten rocks. *J. Geophys. Res.* **85**, 5173–5289.

McKenzie, D. 1984 Generation and compaction of partially molten rock. *J. Petrol.* **25**, 713–765.

Michael, P. J. *et al.* 1994 Mantle control of a dynamically evolving spreading center: Mid-Atlantic ridge 31–34° S. *Earth Planet Science Lett.* **121**, 451–468.

Murase, T. & McBirney, A. R. 1973 Properties of some common igneous rocks and their melts at thigh temperatures. *Geol. Soc. Am. Bull.* **84**, 3563–3592.

Nicolas, A. 1989 *Structure of ophiolites and dynamics of oceanic lithosphere*, p. 367. Deventer: Kluwer.

Nielson, J. E. & Wilshire, H. G. 1993 Magma transport and metasomatism in the mantle: a critical review of current geochemical models. *Am. Mineralogist* **78**, 1117–1134.

O'Connell, R. J. & Budiansky, B. 1977 Viscoelastic properties of fluid-saturated cracked solids, *J. Geophys. Res.* **82**, 5719–5735.

O'Connell, R. J. & Budiansky, B. 1974 Seismic velocities in dry and saturated cracked solids, *J. Geophys. Res.* **79**, 5412–5426.

O'Nions, R. K. & McKenzie, D. 1993 Estimates of mantle thorium/uranium ratios from TH, U and Pb isotope abundances in basaltic melts. *Phil. Trans. R. Soc. Lond.* A **342**, 65–77.

Parmentier, E. M. & Phipps Morgan, J. 1990 The spreading rate dependence of three-dimensional spreading center structure. *Nature* **348**, 325–328.

Phipps Morgan, J. 1987 Melt migration beneath mid-ocean spreading centers. *Geophys Res. Lett.* **14**, 1238–1241.

Phipps Morgan, J. & Forsyth, D. W. 1988 Three-dimensional flow and temperature perturbations due to a transform offset: effects on oceanic crustal and upper mantle structure. *J. Geophys. Res.* **93**, 2955–2966.

Quick, J. E. & Gregory, R. T. 1995 Significance of melt-wall rock reaction: a comparative anatomy of three ophiolites. *J. Geology* **103**, 187–198.

Rabinowicz, M., Nicolas, A. & Vigneresse, J. 1984 A rolling mill effect in the asthenosphere beneath oceanic spreading centers. *Earth Planet. Sci. Lett.* **67**, 97–108.

Sayers, C. 1992 Elastic anisotropy of short-fibre reinforced composites. *Int. J. Solids Structures.* **29**, 2933–2944.

Schmeling, H. 1985 Numerical models on the influence of partial melt on elastic, anelastic and electrical properties of rocks. I. Elasticity and anelasticity. *Phys. Earth Planet. Int.* **41**, 34–57.

Scott, D. & Stevenson, D. 1989 A self-consistent model of melting magma migration, and buoyancy-driven circulation beneath mid-ocean ridges. *J. Geophys. Res.* **94**, 2973–2988.

Sleep, N. H. 1975 Sensitivity of heat flow and gravity to the mechanism of sea-floor spreading. *J. Geophys. Res.* **74**, 542–549.

Sleep, N. H. 1984 Tapping of magmas from ubiquitous mantle heterogeneities: an alternative to mantle plumes? *J. Geophys. Res.* **89**, 10 029–10 041.

Spiegelman, M. 1996 Tracers on the move: the sensitivity of trace element geochemistry to melt transport. *Eos* **76**, 594.

Spiegelman, M. 1993 Physics of melt extraction: theory, implications and applications. *Phil. Trans. R. Soc. Lond.* A **342**, 23–41.

Spudich, P. & Orcutt, J. A. 1980 A new look at the seismic velocity structure of the oceanic crust. *Rev. Geophys. Space Physics* **18**, 627–645.

Takahashi, N. 1992 Evidence for melt segregation towards fractures in the Horoman mantle peridotite complex. *Nature* **359**, 52–55.

Tandon, G. P. & Weng, G. J. 1984 The effect of aspect ratio of inclusions on the elastic properties of unidirectionally aligned composites. *Polymer Composites* **5**, 327–333.

Thomsen, L. 1995 Elastic anisotropy due to aligned cracks in porous rock. *Geophys. Prosp.* **43**, 805–829.

Tolstoy, M., Harding, A. J. & Orcutt, J. A. 1993 Evolution of crustal structure at 34S on the mid-Atlantic ridge. *Eos* **74**, 646.

Toramaru, A. & Fujii, N. 1986 Connectivity of melt phase in a partially molten peridotite. *J. Geophys. Res.* **91**, 9239–9252.

Waff, H. S. & Bulau, J. R. 1982 Experimental studies of near-equilibrium textures in partially molten silicates at high pressure. *Adv. Earth Planet. Sci.* **12**, 229–236.

Waff, H. S. & Faul, U. H. 1992 Effects of crystalline anisotropy on fluid distribution in ultramafic partial melts. *J. Geophys. Res.* **97**, 9003–9014.

Waff, H. S. & Holdren, G. R. 1981 The nature of grain boundaries in dunite and lherzolite xenoliths: implications for magma transport in refractory upper mantle material. *J. Geophys. Res.* **86**, 3677–3683.